J. Fluid Mech. (1985), *vol.* 158, *pp.* 381–398
Printed in Great Britain

Chaotic mode competition in parametrically forced surface waves

By S. CILIBERTO† AND J. P. GOLLUB
Department of Physics, Haverford College, Haverford, PA 19041 U.S.A., and Department of Physics, University of Pennsylvania, Philadelphia, PA 19104 U.S.A.

(Received 24 September 1984 and in revised form 22 February 1985)

Vertical forcing of a fluid layer leads to standing waves by means of a subharmonic instability. When the driving amplitude and frequency are chosen to be near the intersection of the stability boundaries of two nearly degenerate modes, we find that they can compete with each other to produce either periodic or chaotic motion on a slow timescale. We utilize digital image-processing methods to determine the time-dependent amplitudes of the competing modes, and local-sampling techniques to study the onset of chaos in some detail. Reconstruction of the attractors in phase space shows that in the chaotic regime the dimension of the attractor is fractional and at least one Lyapunov exponent is positive. The evidence suggests that a theory incorporating four coupled slow variables will be sufficient to account for the mode competition.

1. Introduction

A variety of recent experiments have demonstrated that the broadband spectra seen in some dissipative hydrodynamic systems are associated with strange attractors. That is, the trajectories representing the dynamics in phase space lie on a complicated attracting set. Chaotic time dependence arises because nearby trajectories diverge from each other exponentially on the average, yet remain within a finite basin of attraction and converge to a zero-volume-limit set (Ruelle 1980; Lanford 1981). These conditions imply that the attractor is folded into an infinite number of layers (hypersurfaces) and is therefore generally an object with fractional dimension. (For a review see Farmer, Ott & Yorke 1983.) The properties of fractional dimension and exponential divergence of nearby trajectories (positive Lyapunov exponent) have been seen in many nonlinear models consisting of three or more coupled ordinary differential equations. Recently, fractional dimension has been demonstrated in experimental studies of circular Couette flow (Brandstater *et al.* 1983), Rayleigh–Bénard convection (Malraison *et al.* 1983), and a differentially heated rotating annulus (Guckenheimer & Buzyna 1983). A positive Lyapunov exponent was found in the Couette-flow experiments, but was not measured in the other cases. Unfortunately, the physical origin of the chaotic states is not yet known. In some cases transition sequences (for example, successive period-doubling in Rayleigh–Bénard convection) can be correlated with the behaviour of simple nonlinear models. However, mathematical models that incorporate the correct dynamics and allow *a priori* prediction of the behaviour as a function of external parameters are not generally available (Miles 1984*a*).

† Permanent address: Istituto Nazionale di Ottica, 50125 Arcetri-Firenze, Largo Enrico Fermi 6, Italy.

In the present paper we consider the standing surface waves excited on a cylindrical fluid layer by a small vertical oscillation of the container, a system first studied by Faraday (1831). The linearly unstable modes are similar to the modes of a drum. We find experimentally that, in a region of parameter space near the intersection of the stability curves for two nearly degenerate modes, both modes can be present simultaneously, and they interact with each other to produce slow oscillations in the surface-wave pattern. These oscillations are chaotic for a certain range of driving amplitude and driving frequency. The observations provide a clear physical mechanism for the onset of chaotic time dependence: mode competition. Although various simplified models of chaotic fluid motion have their basis in the interaction between discrete spatial modes (for example, see Curry 1978), experimental methods capable of providing a time-dependent modal decomposition have not been generally available.

In the experiments reported here we were able to measure the mode amplitudes by a novel application of digital imaging methods in conjunction with time-resolved spatial Fourier analysis. These methods allowed us to determine linear combinations of the time-dependent amplitudes in the modal superposition under certain conditions. We found that the noisy oscillations result from the interaction between only two spatial modes. We also reconstructed the attractors from locally sampled time series, and measured the dimension in the regime of chaotic mode competition. The dynamics can be represented by a fractal attractor of dimension between two and three, the exact value depending on the driving amplitude. Finally, we showed that there is at least one positive Lyapunov exponent.

The experimental observations and available theory suggest that a model consisting of four coupled slow variables can account for the mode competition. However, the derivation of a suitable model from the equations of motion presents significant mathematical difficulties.

This paper extends our preliminary results published earlier (Ciliberto & Gollub 1984). We describe the experimental configuration and the qualitative behaviour of the system in §2. The digital imaging methods used to study mode amplitudes are discussed in §3, with the evidence for mode competition. Measurements based on time series of the locally sampled light intensity, including spectra and reconstructions of the attractors in phase space, are given in §4. The measurements of attractor dimension are presented in §5. Finally, we summarize and discuss our conclusions in §6.

2. Experimental configuration and qualitative behaviour

2.1. *Fluid cell and optics*

The system we have studied is a cylindrical fluid layer about 1 cm deep in a Plexiglas vessel of interior radius $R = 6.35$ cm. (The cell is cylindrical to within about 0.01 cm.) Because surface contamination is known to affect the dissipation of the waves (Miles 1967), we use distilled and de-ionized water that has been passed through both a carbon adsorber to remove organic contaminants and a filter for particulates. Temperature control of the system to within 0.1 °C reduces thermal variations in surface tension and viscosity to an insignificant level.

The fluid cell is mounted on the cone of a loudspeaker in a way that allows vertical forcing with an amplitude of 0–200 μm while still permitting light to be transmitted vertically through the cell (see figure 1*a*). Reasonable precautions are taken to ensure that the oscillation direction and cell axis are vertical. The driving frequency is

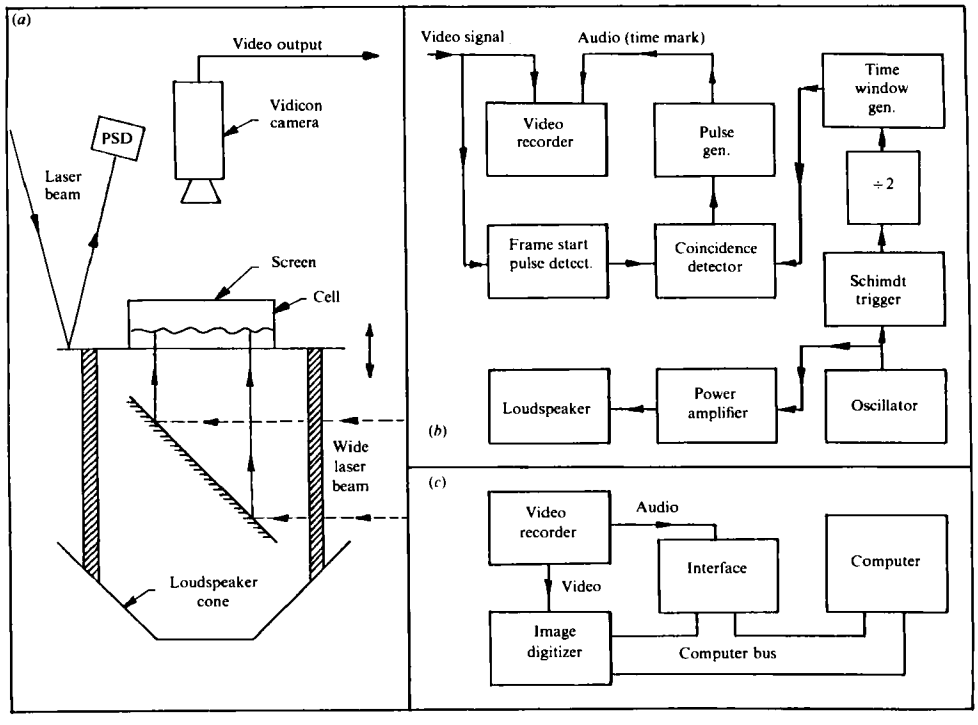

FIGURE 1. (*a*) Schematic diagram of the apparatus. The position-sensing detector (PSD) is used to determine the imposed amplitude of oscillation of the cell. (*b*) Electronics to allow later synchronization of the digitized video signal with the forcing (see §3) by recording of pulses on the audio channel of the video recorder. (*c*) Electronics for video digitization.

derived from a synthesizer and is stable to about 0.001 %. The imposed-oscillation amplitude is measured using a laser beam reflected from a mirror attached to the cell, in conjunction with a position-sensing photodiode. The cell motion is sinusoidal to good accuracy.

Despite our best efforts, we found that the resonant frequencies of the modes of interest tend to drift slowly by as much as 0.3 % in one day. A possible cause is unavoidable variations in the shape of the contact line between the meniscus and vertical wall. These drifts, though slow and small, limit our ability to explore in detail the phenomena of interest, since the region of mode competition is only about 1.5 % wide in driving frequency.

The surface deformation was studied by allowing a parallel (and expanded) laser beam to pass vertically through the cell. The use of a laser gives better collimation than is normally obtained with other sources, but the speckle pattern produced by coherent light has to be avoided. We accomplished this by placing a rapidly spinning translucent disk at the focal point of the beam expander in order to dephase the light. The image formed on a translucent screen located 6 cm above the fluid surface is recorded on videotape and digitized (see §3).

2.2. *Phase diagram*

The linearly unstable modes for the surface displacement have the following form:

$$S_{lm}(r,\theta) = J_l(k_{lm}\, r)\, \sin\,(l\theta + \phi_{lm}), \tag{2.1}$$

where the J_l are Bessel functions of order l. The wavenumber k_{lm} is determined by the boundary condition that the derivative $J_l'(k_{lm} R) = 0$. The modes may be labelled by the indices (l, m), where l is the number of angular maxima and $m-1$ (or m if $l = 0$) is the number of nodal circles. The displacement field may be written as a superposition of these modes with time-dependent coefficients $a_{lm}(t)$ (Benjamin & Ursell 1954):

$$Z(r, \theta, t) = \sum_{l,m} a_{lm}(t)\, S_{lm}(r, \theta). \tag{2.2}$$

(In principle, the phases ϕ_{lm} may also be time dependent. However, for the phenomena described in this paper, they were observed to be time independent, though different from run to run.) A given mode develops a parametric instability when the corresponding eigenfrequency is approximately in resonance with half the driving frequency f_0, and in addition the driving amplitude A exceeds a threshold value A_c. This process leads to standing waves in which the mode amplitude oscillates at $\frac{1}{2}f_0$. To take into account the possibility of a further slow modulation of the mode amplitudes, which in fact occurs owing to mode competition, we write each amplitude in terms of fast oscillations at $\frac{1}{2}f_0$ and slow envelopes $g_{lm}(t)$ and $h_{lm}(t)$:

$$a_{lm}(t) = g_{lm}(t) \cos(\pi f_0 t) + h_{lm}(t) \sin(\pi f_0 t). \tag{2.3}$$

The index m will generally be suppressed when there is no ambiguity.

We explored the behaviour of the system as a function of A and f_0, and identified about 30 modes. As examples, we show images of the (4, 3) and (7, 2) modes in figure 2. These were obtained at a driving amplitude of about $1.1A_c$ (50 μm). The surface is depressed by about 0.5 mm in the dark regions and elevated in the bright regions. These are instantaneous images; one half cycle later the bright and dark regions are interchanged. The (7, 2) mode shown in the figure therefore has seven nodal diameters dividing the circumference into 14 regions of alternating elevation and depression. Although the angular symmetry is obvious from the image, the radial index m is not. However, we were able to determine accurately the radial index by comparing the observed oscillation frequency with the calculated frequencies for modes with the same angular symmetry. Agreement to within about 2% for all 30 modes gave us confidence in our ability to identify modes when only a single one is present. Finally, we note that the images contain a significant amount of fine structure caused in part by capillary waves, and in part perhaps by artifacts of the imaging, since there is not an exact one-to-one correspondence between points on the fluid surface and points on the image plane in shadowgraphs.

The behaviour of the system as a function of A and f_0 is shown in figure 3. This is only a small part of the phase diagram; it covers a range of about 4% in driving frequency that includes the modes of figure 2. We selected this region for detailed study for reasons of experimental convenience, but other regions of the phase diagram also show mode competition. Below the parabolic stability boundaries, the surface is essentially flat, except for a small circularly symmetric response at the driving frequency caused by the meniscus at the outer boundary of the fluid layer. Above the stability boundaries, the fluid surface oscillates at half the driving frequency in a single stable mode. The shaded areas are regions of mode competition, in which the surface can be described as a superposition of the (4, 3) and (7, 2) modes with amplitudes having a slowly varying envelope in addition to the fast oscillation at $\frac{1}{2}f_0$. These slow variations can be either periodic with a typical period of about 15 s, or chaotic (see §4). The boundary of the periodic region seems to be non-hysteretic, and the transition there is continuous. This may be contrasted with the line separating

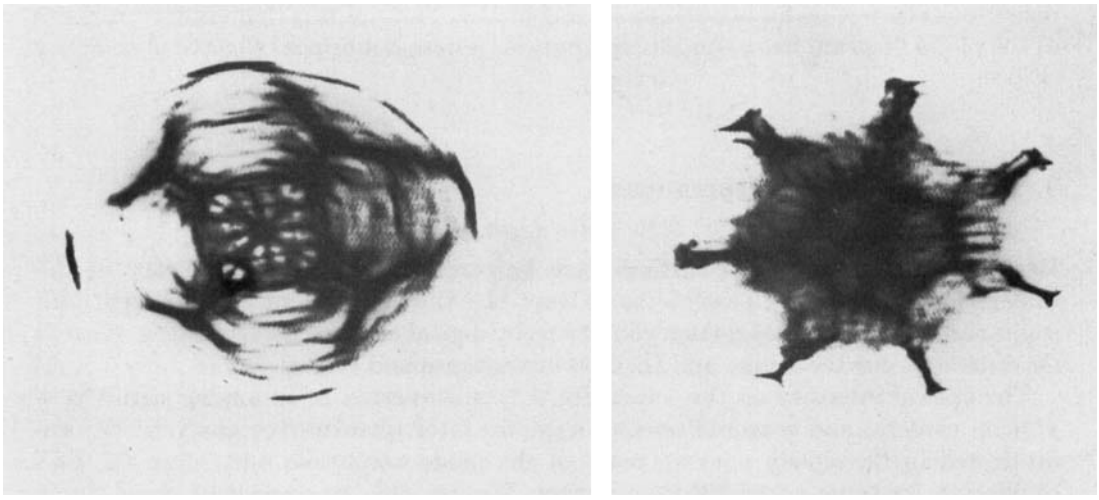

FIGURE 2. Optical-intensity patterns for the (4, 3) and (7, 2) modes, respectively. The first index gives the number of angular maxima.

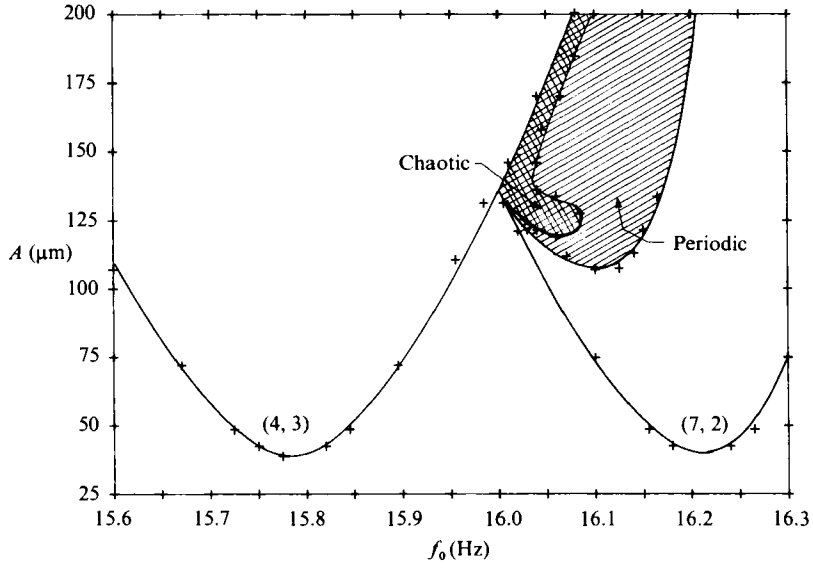

FIGURE 3. Phase diagram as a function of driving amplitude A and frequency f_0. The crosses are experimentally determined points on the stability boundaries. Stable patterns occur in the regions labelled (4, 3) and (7, 2). Slow-periodic and chaotic oscillations involving competition between these modes occur in the shaded regions.

the periodic and chaotic regions, which does show some hysteresis (possibly caused by pinning of the contact line). It is drawn for increasing A in figure 3.

At driving amplitudes higher than those shown in figure 3 the surface can become chaotic even if the driving frequency is resonant, so that a single mode is dominant. A study of some of these phenomena (involving the breakdown of a single mode) has been given by Gollub & Meyer (1983). In the present paper, we focus our attention on the regions of mode competition near the intersections of the stability boundaries.

We note that the boundary of the *higher*-frequency mode ends where the two lines intersect, while the boundary of the lower-frequency mode continues. The same

behaviour also occurs for other intersecting modes. Perhaps this elementary property of the phase diagram has a simple explanation; it does not appear to have been noted before.

3. Digital imaging measurements

3.1. *Video digitization*

Because the images of the surface-wave patterns preserve the symmetry of the underlying modes, it is possible to extract the time-dependent mode amplitudes semiquantitatively under certain conditions by digital analysis of the images. We will describe first our technique and then its advantages and limitations.

The optical intensity on the screen $I(r, \theta, t)$ is converted to an analog signal by a vidicon camera, and is stored on videotape for later quantitative analysis. We are interested in the slowly varying parts of the mode amplitude $a_l(t)$, since the fast oscillation contains no useful information. We are able to measure a *fixed linear combination* $a_l^0(t)$ of the slow coefficients $g_l(t)$ and $h_l(t)$ by synchronizing the digitization of the video signal with the vertical acceleration of the fluid. (It would be better to measure the slow coefficients independently, but this would be much more complicated.) We accomplished this as follows. The frame-start pulse is extracted from the video signal and compared with the phase of the driving oscillator. When these are coincident (within a selected window) a pulse is sent to the *audio* channel of the video recorder. This process is shown schematically in figure 1(*b*). When the tape is later played back for digitization of the image, the pulses on the audio channel are used to determine which video frames have the proper phase to acquire.

Images from the tape are digitized by a fast 8-bit analog-to-digital converter (figure 1*c*) that resides on the bus of an LSI 11/23 computer. The frame grabber and frame store (separate from the computer memory) are special-purpose boards manufactured by Datacube, Inc. Software to drive them and process the results was written in our laboratory. The result of digitization is a 320×240 point array representing the intensities in the image plane. Typically, there are about 6 or 7 bits of useful information (signal-to-noise ratio of about 100) in each point. Each frame represents information recorded in $\frac{1}{60}$ s, a time that is significant in comparison with the period of the fast oscillation at $\frac{1}{2}f_0$ (typically 7–10 Hz). Therefore, there is some (but not too much) time averaging of the wave pattern.

The phenomena of interest concern the competition between two modes of different *angular* symmetry. This fact allows us to integrate the digitized light-intensity field over radial segments to obtain a *one-dimensional* intensity function $I(\theta, t)$ for angular Fourier analysis. This averaging operation both reduces noise and simplifies the data analysis. Tests of reproducibility of the data show that the r.m.s. variation of this function from one picture to another is only 0.5% when a narrow time window of 100 μs is used for synchronization of the data acquisition. If the time window is widened to 7 ms (sometimes necessary to obtain a sufficient number of coincidences when the pattern is changing rapidly) the r.m.s. variation increases to 4%. Thus, the digital imaging measurements are quite reproducible. The question of accuracy is considered in §3.2.

There is one further experimental difficulty associated with the digital imaging method: spatial variations in the illumination cause the measured intensity to have a spurious gradual angular variation. The measured intensity is approximately the product of a slowly varying background function and a rapidly varying function

related to the surface waves. We remove the background function by division before further processing and denote the resulting corrected intensity function by $\tilde{I}(\theta, t)$.

3.2. *Measurement of time-dependent mode amplitudes*

To obtain the relative contributions of different values of l we calculate the magnitude squared of the complex Fourier series for the angular intensity function $\tilde{I}(\theta)$ at each time step. The height of this angular spectrum $P(l)$ at a given l is approximately proportional to the square of the slowly varying amplitude $a_l^0(t)$. (Recall that $a_l^0(t)$ is a fixed linear combination of $g_l(t)$ and $h_l(t)$ with coefficients that depend on the timing of the data acquisition with respect to the forcing.) The constants of proportionality depend on radial integrals of the J_l.

Thus, this method allows an approximate time-resolved normal-mode analysis under certain conditions. The major limitation of the method is that the optical-intensity field is not linear in the surface-wave height. This is not an overwhelming difficulty because the main qualitative effect is to create spurious spatial harmonics, which can be easily ignored. But the measurement nonlinearities also mean that conclusions depending on the precise shape of the functions $a_l^0(t)$ cannot be drawn. This limitation is not serious in the present paper, but might be in other circumstances. If necessary the nonlinearities could possibly be measured and corrections applied. We have not done a quantitative study of this problem, which is known to be a difficult one.

As an example of the application of this method to the problem at hand, we show in figure 4 the angular-intensity functions and corresponding power spectra for two times during the process of competition between the (4, 2) and (7, 3) modes. In (*a*) the pattern is dominated by the sevenfold mode. There are seven angular maxima, and the dominant spectral peaks are at $l = 7$ and 14. (The latter is probably due to a mixture of real-harmonic generation and imaging nonlinearity.) However, there is also a small peak at $l = 4$ corresponding to the admixture of a small amount of the fourfold mode into the surface displacement.

We find that in the shaded region of the phase diagram (figure 3) the angular-intensity pattern and relative spectral heights are time dependent. For example, in figure 4 (*b*), taken a few seconds later, the dominant spectral peaks are those for $l = 4$ and 8. The line at $l = 7$ cannot be resolved because it is small and too close to the harmonic of the fourfold mode at $l = 8$. By doing angular Fourier analysis at many times and plotting the square roots of the spectral heights $P(7)$ and $P(4)$, we obtain (approximately, and up to a constant of proportionality) the time-dependent mode amplitudes $a_7^0(t)$ and $a_4^0(t)$. These functions are shown in figure 5. The slow oscillation is periodic in this case with a period of 15 s. The period is about two orders of magnitude larger than that of the fast oscillation at $\frac{1}{2}f_0$. We find that $a_7^0(t)$ leads $a_4^0(t)$ by about 90°. This phase difference and qualitative visual observations indicate that energy is being transferred back and forth between the two modes. These results of the digital-imaging measurements are the basic quantitative evidence for our assertion that the slow oscillations are caused by competition between two spatial modes.

Our method, based on shadowgraph imaging and one-dimensional (time-resolved) spatial Fourier analysis, is somewhat limited in its range of applicability. However, it does appear to be novel in allowing time-dependent mode amplitudes to be measured semiquantitatively. If suitably extended to a full two-dimensional normal-mode analysis, this type of measurement should have wide applicability.

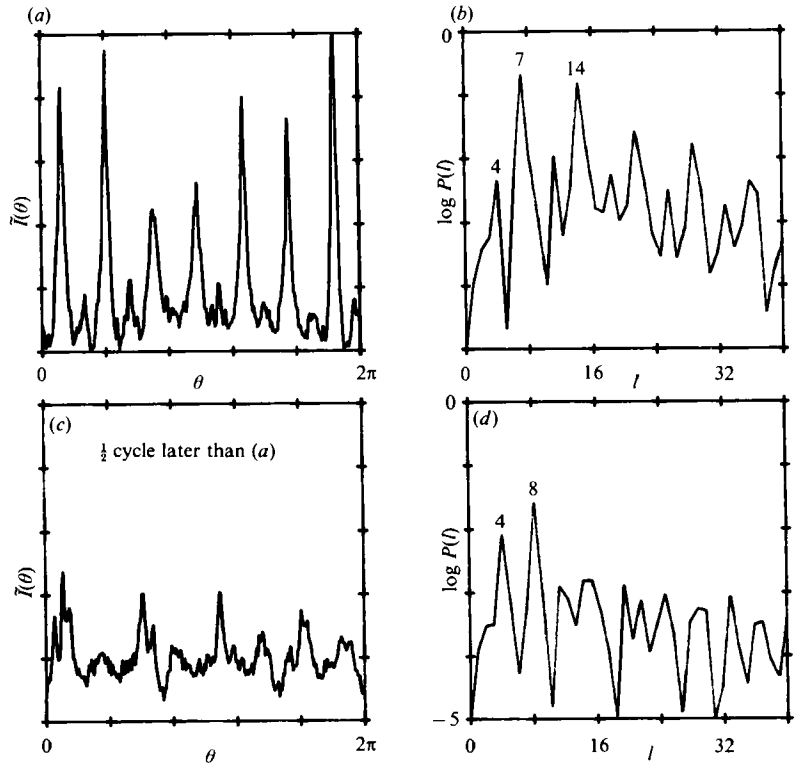

FIGURE 4. Time-resolved spatial Fourier analysis is illustrated by (*a*) the angular-intensity pattern $\tilde{I}(\theta)$ and (*b*) the corresponding angular power spectrum $P(l)$ for an oscillatory state in which the $l = 7$ and 4 modes are both present. Spectral peaks corresponding to harmonics of these modes are also substantial. The relative peak heights in the angular spectrum oscillate so that at a later time, as shown in (*c*) and (*d*), the fourfold mode is dominant, while the sevenfold mode is not visible.

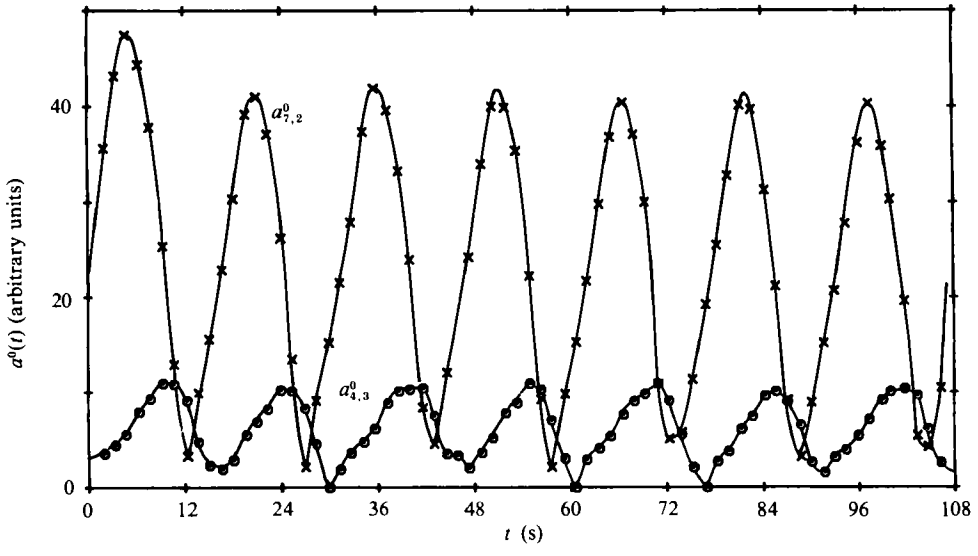

FIGURE 5. Mode competition. The slowly varying mode amplitudes $a^0_4(t)$ and $a^0_7(t)$ oscillate periodically for $f_0 = 16.113$ Hz. Chaotic oscillations are found at lower driving frequencies.

4. Time-series analysis and visualization of the attractors

The digital imaging technique could be used to study the dynamics of the slow oscillation. However, it requires *spatial* Fourier analysis at each time step, a rather laborious process involving tremendous amounts of data (about 10^8 bytes for a minimal time series of 1000 points). Therefore, we use a different method for detailed studies of the mode competition. We monitor the time dependence by measuring the light intensity $V(t)$ at a single point in the image as a function of time instead of digitizing the entire pattern. Although this provides no spatial information the signal-to-noise ratio is substantially better than can be obtained from a vidicon camera, a fact that allows us to both reconstruct the shape of the attractor and obtain high-quality power spectra.

(One possible objection to local sampling is that any rotation of the pattern would be an additional source of time dependence distinct from that provided by mode competition. However, our experience is that rotational motion does not occur, perhaps because of small unavoidable asymmetries in the shape of the contact line at the outer wall.)

The local light intensity is monitored by a photodiode, and the fast component associated with the oscillation at half the driving frequency is eliminated by lock-in detection. We digitize with 12-bit resolution, but the actual precision is about one part in 800. The sampling time is adjusted to provide 50 samples per oscillation period (10 s) for plotting trajectories in phase space, and about 6 samples per oscillation period for spectra and dimension measurements.

4.1. *Spectra*

The interaction region of the phase diagram was explored by varying A and f_0 separately. In both cases, as one crosses from the region of slow periodic oscillations into the chaotic region, one finds a period-doubling bifurcation followed (or accompanied) by a transition to chaos. A typical example is shown in figure 6, where time series are shown for three different driving amplitudes but fixed driving frequency of 16.05 Hz. In addition, power spectra of the time series are computed using standard fast-Fourier-transform methods and are shown on a logarithmic scale in figure 6.

At a driving amplitude of 121 μm (figures 6*a*, *b*) the slow oscillation is periodic and the spectrum has a single sharp peak at a frequency f^* and harmonics. However, a subharmonic bifurcation occurs at $A = 139$ μm. At 149 μm this subharmonic is seen clearly both in the signal and in the spectrum (figures 6*c*, *d*). A detectable increase in the noise level, and a slight broadening of the peaks, accompanies the growth of the subharmonic. Beyond 180 μm the time record is clearly chaotic, as shown in figures 6(*e*, *f*). The spectral peaks (shifted slightly to the left) are quite broad, and the background noise level is high. There is some evidence of a second (noisy) subharmonic bifurcation with a broad spectral peak near $\frac{1}{4}f^*$ and harmonics. We are unable to tell whether the growth of noise illustrated in figure 6 is entirely continuous: it might possibly involve a discontinuous jump. At amplitudes higher than 200 μm there is no mode competition. The oscillations disappear and only the fourfold symmetric mode is present.

Note that this transition sequence is not the only possible one. As indicated by the structure of the parameter space (figure 3) it is possible to go directly to chaos from the pure (4, 3) mode simply by decreasing the driving amplitude.

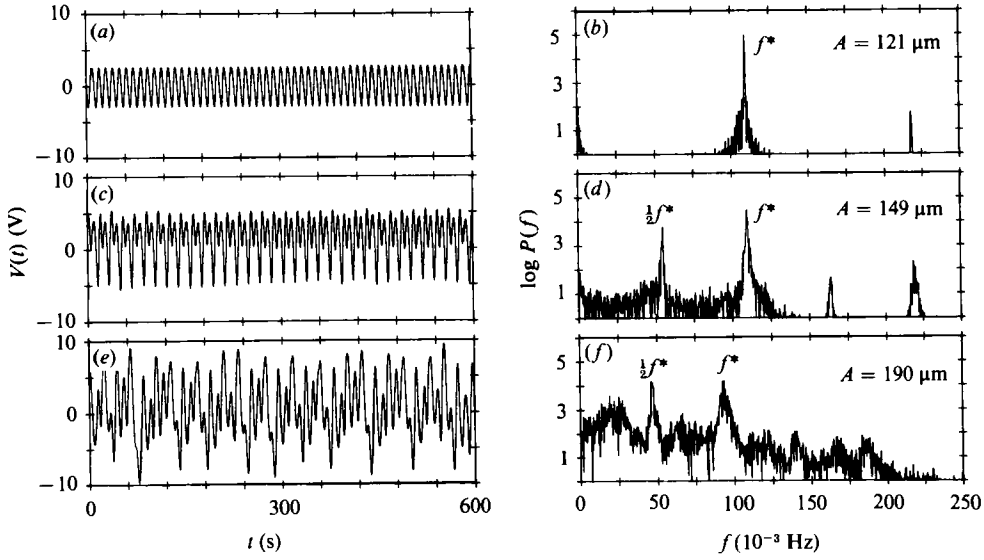

FIGURE 6. The transition from periodic to chaotic oscillation. Time series and corresponding power spectra of the slowly varying part of the local light intensity are shown for $f_0 = 16.05$ Hz and three different driving amplitudes. Broadband noise is associated with the appearance of a subharmonic $\frac{1}{2}f^*$ of the dominant oscillation.

4.2. *Phase portraits*

The behaviour illustrated in figure 6 is certainly *suggestive* of the existence of a strange attractor since the transition seems to involve a subharmonic bifurcation (a common nonlinear process), and we know that only two spatial modes are present. In order to visualize the attractor we construct phase portraits by embedding the trajectories in an m-dimensional phase space as suggested by Packard *et al.* (1980) and Takens (1981), and found to be useful in other experiments (Brandstater *et al.* 1983). We choose phase-space coordinates $\{V(t), V(t+\tau), \ldots, V(t+(m-1)\tau)\}$, where τ is an arbitrary delay. The phase portraits constructed in this way generally have the same dynamical properties as those constructed from a set of more logically chosen independent variables (Grassberger & Procaccia 1983*a*). In our case, these preferred variables might be the amplitudes $g_l(t)$ and $h_l(t)$ of the two spatial modes. The embedding method depends on the fact that in a nonlinear system all variables are effectively coupled. However, it is basically a way of extracting information from a single time series that would be provided more ideally from precise measurements of all of the mode amplitudes. Hence it should be used with caution.

The results of a two-dimensional recosntruction are shown in figures 7(*a*), (*b*) for the data reported in figure 6. These phase portraits may also be regarded as projections of higher-dimensional phase portraits on the plane defined by $V(t_n+\tau)$ and $V(t_n)$. In these figures, the delay τ is 3 s and the sampling time is 0.2 s. In order to obtain a sensible reconstruction the sampling time must be very short compared with the basic oscillation period T, while the delay time should be only somewhat less than T. (The reconstruction process has been studied empirically by Roux, Simoyi & Swinney 1983.) If the delay time is taken to be too small the attractor becomes compressed along the diagonal, and the structure cannot be seen. We varied the delay time in order to obtain an optimal representation of the data.

The first portrait (figure 7*a* which corresponds to the data of figure 6*a*) is obviously

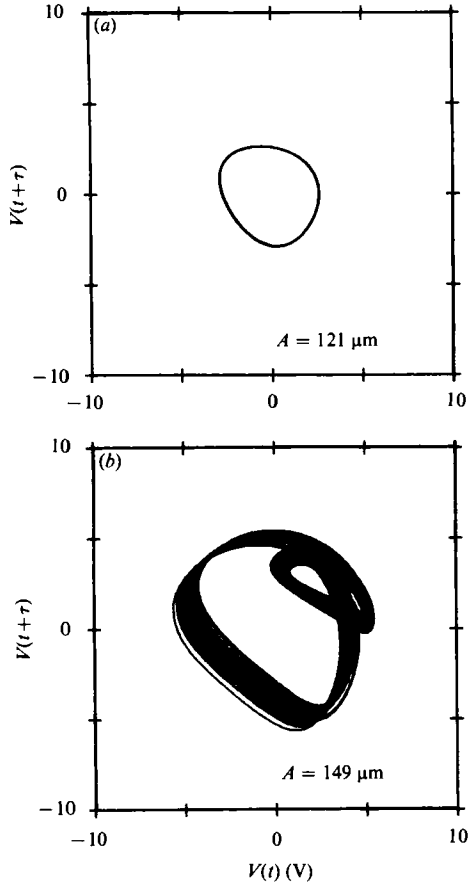

FIGURE 7. Phase portraits corresponding to the top two panels of figure 6. The first one is clearly a limit cycle. The second shows a subharmonic (extra loop) but is also noisy.

a limit cycle. The second one (figure 7*b* corresponding to figure 6*c*) shows the subharmonic bifurcation and also some noise. It is not immediately obvious whether this should be regarded as intrinsic dynamical noise or noise owing to amplified external perturbations. It is definitely much larger than the measurement noise. Finally, we show in figure 8(*a*) the phase portrait for the strongly chaotic state at $A = 190$ μm (corresponding to figure 6*e*). Here, the trajectories are spread over the plane. By following visually a swath of closely spaced lines one can see qualitatively the strong divergence of nearby trajectories that is characteristic of a strange attractor.

Two dimensions are clearly inadequate because trajectories cross. Therefore, we constructed three-dimensional phase portraits and then observed intersections (Poincaré sections) with a plane defined by the condition $V(t) = V(t+\tau)$. The result is shown in figure 8(*b*) for the strongly chaotic state. (Only the crossings in one direction are used.) The points fall along a number of lines, suggesting that the actual orbits lie on many sheets. This multi-sheeted geometry is another hallmark of a strange attractor.

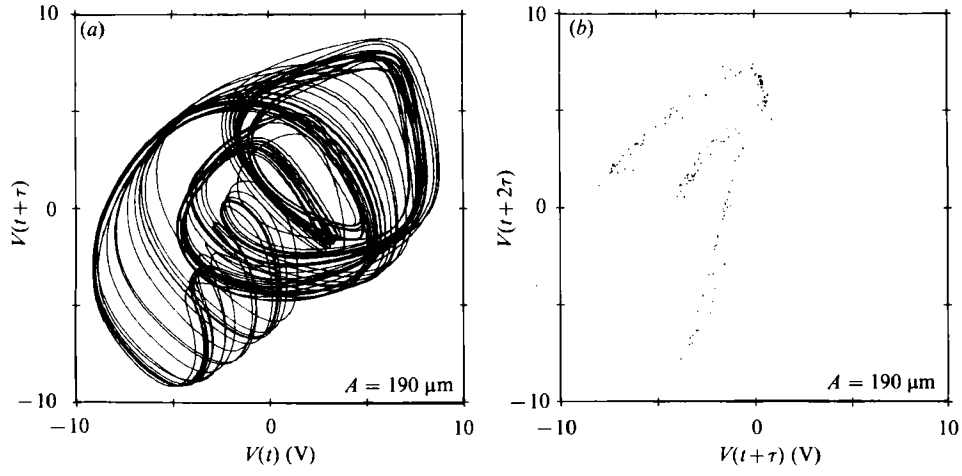

FIGURE 8. Phase portrait and corresponding Poincaré section for the noisy data in the lower panel of figure 6. Divergence of nearby orbits can be seen qualitatively in the phase portrait, while the map shows that the attractor has several sheets.

5. Dimension measurements

5.1. *Background*

One of the most distinctive characteristics of a strange attractor is that it is (almost always) an object of fractional dimension. This means that the number of cells of size ϵ needed to cover the attractor scales as ϵ^{-D} in the limit of small ϵ, where D, the fractal dimension, is generally not an integer. (For simple objects D coincides with the ordinary Euclidean dimension, as the reader may easily check.) Qualitatively, this is a reflection of the fact that a chaotic attractor is a complex structure with much open space; its intersection with a line often forms a Cantor set.

Measurement of D is a useful way to characterize the degree of chaos, and the results may suggest an appropriate model. Although it is very difficult to obtain D from an experiment several other definitions of dimension do lead to practical prescriptions for measurement. The information (or pointwise) dimension d may be computed from the fact that the number of points $S(\epsilon)$ contained in an m-dimensional ball of radius ϵ scales as ϵ^d on the average (Farmer *et al.* 1983). More precisely,

$$d = \lim_{\epsilon \to 0} \frac{\langle \log S(\epsilon) \rangle}{\log \epsilon}. \tag{5.1}$$

To measure d it is sufficient in principle to compute $S(\epsilon)$ for a ball centred at a particular point on the attractor, average its logarithm over a sufficient number of points on the attractor, plot $\langle \log S(\epsilon) \rangle$ *versus* $\log \epsilon$, and determine the slope. It is necessary, however, to vary the embedding dimension m, since it is not known in advance how large a value is necessary. Once m is sufficiently large, making it larger does not change d (except for statistical fluctuations).

A second quantity known as the correlation dimension ν (Grassberger & Procaccia 1983*a*) can also be easily measured. It is defined in terms of a quantity $C(\epsilon)$, the number of pairs of data points whose separation in phase space is less than ϵ (divided

by N^2, where N is the total number of data points). For large N this quantity scales as ϵ^{ν}, so that one can define ν as follows:

$$\nu = \lim_{\epsilon \to 0} \frac{\log C(\epsilon)}{\log \epsilon}. \tag{5.2}$$

The various dimensions satisfy the inequalities $\nu \leqslant d \leqslant D$. In most cases that have been tested, however, these different ways of defining dimension give almost identical results.

In order to characterize the attractors observed in our experiments we have measured the dimension as a function of driving amplitude. We used files of 2048 points with a sampling time of 1.5 s, and a delay time for embedding of 1.5 s. The sampling time must be longer for the dimension calculation than for the plotting of phase portraits in order to obtain a greater number of orbits (about 300) and hence fill out the attractor more thoroughly. We varied the delay time in order to obtain as large a scaling range for $S(\epsilon)$ or $C(\epsilon)$ as possible. We find that the results are not appreciably different for shorter data files of 1024 points, although statistical fluctuations are greater. Files larger than 2048 points can be used, but computations are then excessively time consuming (more than a few hours on an LSI 11/23 computer). The computation times required to obtain d and ν are comparable.

5.2. *Results of dimension measurements*

The function $N^2C(\epsilon)$ for the strongly chaotic data of figures 6(*e*, *f*) is shown in figure 9 on logarithmic scales for various values of the embedding dimension. We show the same information more sensitively in figure 10(*a*), where the derivative of $\log C(\epsilon)$ is plotted. The slope can be seen to reach a limiting value in the scaling region (near $\log \epsilon = -1$) that does not increase once m is larger than about 4. This tells us that a phase-space dimension of 4 is sufficient to represent this data. The limiting value of the slope, i.e. the height of the plateau in figure 10(*a*), is 2.20 ± 0.04. This is the correlation dimension ν of the attractor (at $A = 190$ μm) in the chaotic regime.

The range of scaling behaviour (region of constant slope) is limited on the high end by the size of the attractor, and on the low end by instrumental noise. When ϵ becomes so small that it is comparable with the noise, the slope rises to a value roughly equal to the embedding dimension. As proposed by Ben-Mizrachi & Procaccia (1984) this is an excellent way to distinguish between environmental or measurement noise and fluctuations that are intrinsic to the dynamics of the strange attractor (chaos). The former will cause the full dimension of the available phase space to be utilized on small scales, and hence leads to a non-saturating slope at low ϵ. These regions are clearly separable in figure 10(*b*), where measurement noise dominates for $\log \epsilon < -1$. This method of distinguishing chaos from random noise was studied by Brandstater & Swinney (1984).

We have also computed the function $\langle \log S(\epsilon) \rangle$ to obtain the information dimension. The derivative of $\langle \log S(\epsilon) \rangle$ is shown in figure 10(*b*). The slope saturates at a value of $d = 2.22 \pm 0.04$ for $m \geqslant 4$ in the scaling region. (However, the behaviour for small ϵ is different for the two methods. We find that the information method is more sensitive to statistical fluctuations and requires longer data sets to exhibit the behaviour at small ϵ properly.) The two methods are seen to give essentially identical results. The correlation dimension ν and information dimension d are equal to within the accuracy of the measurements.

We measured the dimensions for lower driving amplitudes as well. In the regime of periodic oscillation they are approximately unity, as one would expect for a limit

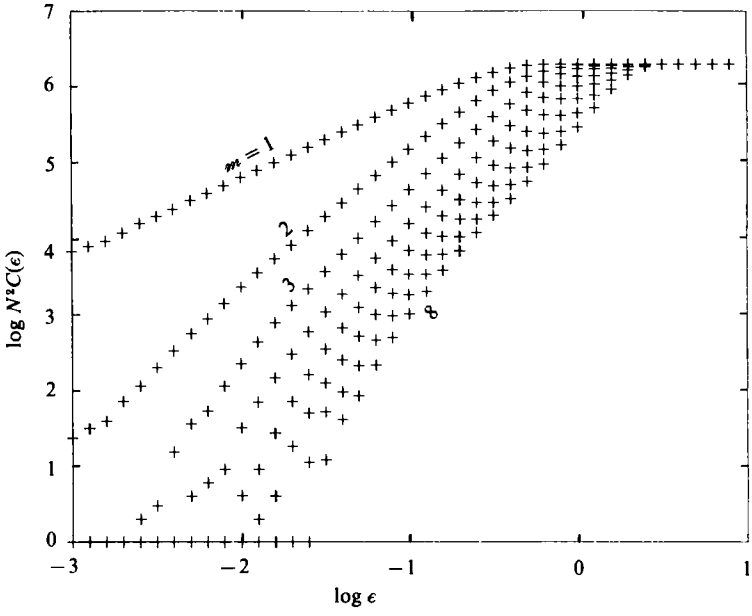

FIGURE 9. The correlation function $C(\epsilon)$ for various values of the embedding dimension m. The limiting slope for large m is the correlation dimension ν of the attractor.

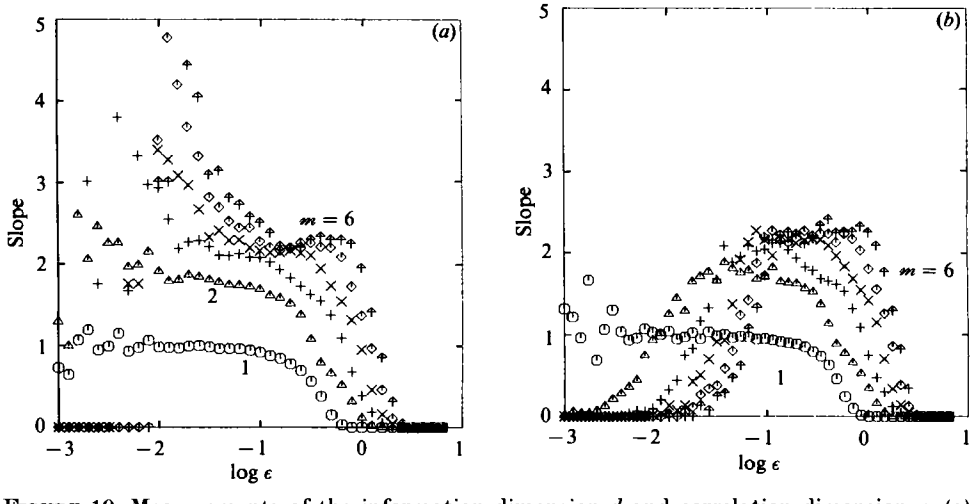

FIGURE 10. Measurements of the information dimension d and correlation dimension ν. (*a*) The derivative (local slope) of the function $\log C(\epsilon)$ with respect to $\log \epsilon$ reaches a limiting value in the scaling range of $d = 2.20 \pm 0.04$ for $m \geqslant 4$. (*b*) The derivative of the function $\langle \log S(\epsilon) \rangle$ behaves in the same way (except at low ϵ, as explained in the text).

cycle. Just above the noisy subharmonic bifurcation we are unable to make a reliable measurement because the trajectories are so close together (figure 7*b*) that much longer files would be needed to obtain adequate statistics.

5.3. *Positive Lyapunov exponent*

There is no way to obtain a fractal attractor without at least one positive Lyapunov exponent, corresponding to stretching of displacements in one locally defined

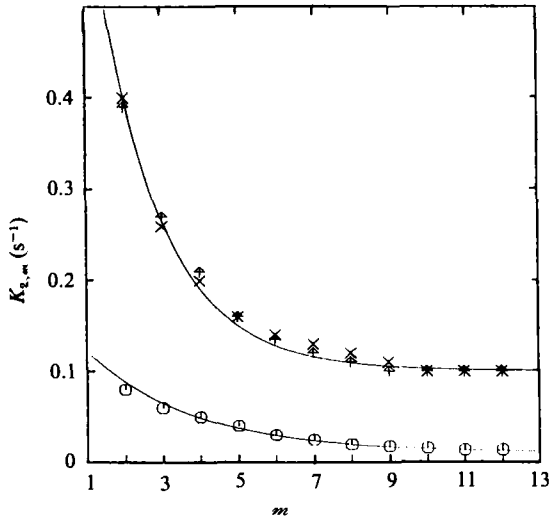

FIGURE 11. Dependence on embedding dimension of the function $K_{2,m}$ (defined in (5.3)), which is less than or equal to the sum of the positive Lyapunov exponents. The curves are fits to the data for the chaotic state (upper points) and periodic state (lower points), for $\log \epsilon = -1$. The positive limit of the upper curve for large m demonstrates that at least one Lyapunov exponent must be positive, so that the trajectories exhibit exponential divergence.

direction in phase space. It is possible to make a quantitative estimate of the degree of stretching or sensitive dependence on initial conditions (Grassberger & Procaccia 1983*b*). The curves of $\log C(\epsilon)$ for different values of the embedding dimension m are parallel but displaced vertically from each other (see figure 9). One may define a quantity $K_{2,m}$ as follows:

$$K_{2,m} = \frac{\log C_m - \log C_{m+1}}{\tau}. \tag{5.3}$$

This quantity should reach a definite limit K_2 for large m, and ϵ in the scaling range; it is known to be less than or equal to the sum of the positive Lyapunov exponents.

Data for $K_{2,m}$ in the strongly chaotic state (figures 6*e*, *f*) and $\log \epsilon = -1$ are shown in the upper part of figure 11 by the crosses. (The triangles are computed using $\langle \log S_m(\epsilon) \rangle$ instead of $\log C_m(\epsilon)$ in (5.3), with essentially identical results.) Similar data are shown for the periodic regime (figures 6*a*, *b*) in the lower part of figure 11. In order to determine the large-m limit, we fitted the data in each case to the following function:

$$K_{2,m} = K_2 + A \exp\left(\frac{-m}{m_0}\right). \tag{5.4}$$

The fits are shown by the solid lines. We found $K_2 = 0.1 \pm 0.01$ s^{-1} in the chaotic state. (Within the scaling range, the variation with ϵ is of the order of the indicated uncertainty.) This means that *at least* one Lyapunov exponent is positive. If *exactly* one Lyapunov exponent is positive (i.e. trajectories diverge in a single locally defined direction, but not in other directions) then it must be this large. We may estimate that two trajectories initially displaced by a sufficiently small amount in this direction will separate on the average by a factor of e^1 in 10 s, which is the mean period of motion on the attractor. In contrast, $K_2 = 0.01 \pm 0.01$ s^{-1} in the periodic state. Thus there is no stretching of trajectories in the periodic state.

6. Summary and conclusion

6.1. *Main results*

We list here the major results of this investigation:

1. We extend previous experimental work on surface waves in a vertically oscillating fluid layer. Regions of mode competition occur (figure 3) in which the wave pattern oscillates either periodically or chaotically with a period long compared with that of the forcing.

2. We use digital imaging methods and time-resolved spatial Fourier analysis to measure the slow mode amplitudes $a_l^0(t)$, which are fixed linear combinations of the slow coefficients defined in (2.3). They oscillate with a phase difference of about 90° on the slow timescale.

3. We study the transition to chaos by a local-sampling technique. Power spectra (figure 6) reveal that the noise onset involves a single subharmonic bifurcation of the slow variables. Phase portraits and Poincaré maps (figures 7 and 8) allow the attractors to be visualized.

4. Dimension measurements (figures 9 and 10) demonstrate that, over the observable range of scales, the attractor is an object of fractional dimension close to 2.2 in the regime of chaotic mode competition. The dimension of the attractor depends weakly on the driving amplitude. A four-dimensional phase space is required to represent the data.

5. The data also show that there must be at least one positive Lyapunov exponent (figure 11) so that nearby trajectories diverge from each other exponentially on the average. Therefore, the chaotic mode competition is appropriately described as a strange attractor.

6.2. *Discussion*

One novel feature of this investigation is the direct measurement of mode amplitudes in a hydrodynamic system using digital image-processing techniques. We believe that this is a technique with wide applicability to a variety of systems. However, for many applications it will be necessary to find optical methods that are more closely related to the hydrodynamic variables than is the case for the shadowgraph approach used here. For example, one might study interfacial waves at the boundary between a transparent fluid and an optically absorbing fluid with the same index of refraction. The interfacial-displacement field might then be determined directly from the optical-intensity field.

In many studies of hydrodynamic chaos the spatial structure of the flow is not known. Here, however, we know that the chaotic behaviour is caused by competition between two of the normal modes of the system. It should be possible to use this information to derive a coupled-mode model from the equations of motion of the system, perhaps along the lines suggested by Miles (1984*b*). Despite the apparent simplicity of the physical phenomena the mathematical difficulties seem to be substantial.

In order to summarize the data from a purely empirical point of view we considered phenomenological models based on the fact that each mode amplitude $a_l(t)$ follows a Mathieu equation in a linearized inviscid approximation (Benjamin & Ursell 1954). We coupled two Mathieu oscillators after introducing damping and cubic nonlinearity. We found that one model of this type, with suitable choices for the parameters, could represent many of the experimental results fairly well including the qualitative structure of the parameter space (figure 3), the route to chaos (figure 6), and the

dimension of the resulting strange attractor. However, the shapes of the stability boundaries were significantly different from those determined experimentally, and certain aspects of the model lack theoretical justification. This model has been described elsewhere (Ciliberto & Gollub 1984, 1985).

The theoretical literature on this problem of vertically forced surface waves seems quite limited in comparison with the extensive literature on models for Rayleigh–Bénard convection patterns. Although surface-wave problems are difficult we believe that more can be done to develop useful model systems by suitable approximations to the equations of motion.

Many questions remain for future work. For example, do all nearly degenerate modes compete, or only those with certain symmetry properties? How does the flow become *spatially* chaotic? What happens at higher driving frequencies, where the density of modes is much greater?

This work was supported by National Science Foundation Grant CME-8310933. S. Ciliberto acknowledges the support of an Angelo della Riccia fellowship during his tenure at Haverford College. J. P. Gollub appreciates the assistance of a Guggenheim Fellowship. Much of the digital imaging software that was essential for this work was written by P. Fraenkel. We acknowledge helpful discussions with J. Guckenheimer, T. Lubensky, J. Miles, I. Procaccia, and H. Swinney, and technical assistance by T. Davis at Haverford.

REFERENCES

Brandstater, A., Swift, J., Swinney, H. L., Wolf, A., Farmer, J. D., Jen, E. & Crutchfield, J. P. 1983 Low dimensional chaos in a hydrodynamic system. *Phys. Rev. Lett.* **51**, 1442–1445.

Brandstater, A. & Swinney, H. L. 1984 Distinguishing low-dimensional chaos from random noise in a hydrodynamic experiment. In *Fluctuations and Sensitivity in Nonequilibrium Systems* (ed. W. Horsthemke & D. Kondepudi). Springer.

Ben-Mizrachi, A., Procaccia, I. & Grassberger, P. 1984 The characterization of experimental (noisy) strange attractors *Phys. Rev.* A **29**, 975–977.

Benjamin, T. B. & Ursell, F. 1954 The stability of the plane free surface of a liquid in vertical periodic motion. *Proc. R. Soc. Lond.* A **225**, 505–515.

Ciliberto, S. & Gollub, J. P. 1984 Pattern competition leads to chaos. *Phys. Rev. Lett.* **52**, 922–925.

Ciliberto, S. & Gollub, J. P. 1985 - Phenomenological model of chaotic mode competition in surface waves. *Nuovo Cim. B*, in press.

Curry, J. H. 1978 A generalized Lorenz system. *Commun. Math. Phys.* **60**, 193–204.

Faraday, M. 1831 On the forms and states assumed by fluids in contact with vibrating elastic surfaces. *Phil. Trans. R. Soc. Lond.* **121**, 319–340.

Farmer, J. D., Ott, E. & Yorke, J. A. 1983 The dimension of chaotic attractors. *Physica* D **7**, 153–180.

Gollub, J. P. & Meyer, C. W. 1983 Symmetry-breaking instabilities on a fluid surface. *Physica* D **6**, 337–346.

Grassberger, P. & Procaccia, I. 1983*a* Measuring the strangeness of strange attractors. *Physica* D **9**, 189–208.

Grassberger, P. & Procaccia, I. 1983*b* Estimation of the Kolmogorov entropy for a chaotic signal. *Phys. Rev.* A **28**, 2591–2593.

Guckenheimer, J. & Buzyna, G. 1983 Dimension measurements for geostrophic turbulence. *Phys. Rev. Lett.* **51**, 1438–1441.

Lanford, O. E. 1981 Strange attractors and turbulence. In *Hydrodynamic Instabilities and the Transition to Turbulence* (ed. H. L. Swinney & J. P. Gollub), pp. 7–26. Springer.

MALRAISON, B., ATTEN, P., BERGÉ, P. & DUBOIS, M. 1983 Dimension of strange attractors: an experimental determination for the chaotic regime of two chaotic systems. *J. Phys. Lett.* (*Paris*) **44**, L897–L902.

MILES, J. 1967 Surface-wave damping in closed basins. *Proc. R. Soc. Lond.* A **297**, 459–475.

MILES, J. 1984*a* Strange attractors in fluid dynamics. *Adv. Appl. Mech.* **24**, 189–214.

MILES, J. 1984*b* Nonlinear Faraday resonance. *J. Fluid Mech.* **146**, 285–302.

PACKARD, N. H., CRUTCHFIELD, J. P., FARMER, J. D. & SHAW, R. S. 1980 Geometry from a time series. *Phys. Rev. Lett.* **45**, 712–715.

RUELLE, D. 1980 Strange attractors. *Math. Intelligencer* **2**, 126–137.

ROUX, J.-C., SIMOYI, R. H. & SWINNEY, H. L. 1983 Observation of a strange attractor. *Physica* D **8**, 257–266.

TAKENS, F. 1981 Detecting strange attractors in turbulence (ed. D. A. Rand & L. S. Young). Lecture Notes in Mathematics vol. 898, Springer.